

## Splitting of the $p$ orbit in triaxially deformed ${}_{\Lambda}^{25}\text{Mg}$

Masahiro Isaka and Masaaki Kimura

*Department of Physics, Hokkaido University, Sapporo 060-0810, Japan*

Akinobu Doté

*Institute of Particle and Nuclear Studies, KEK, Tsukuba, Ibaraki 305-0801, Japan and  
J-PARC Branch, KEK Theory Center, IPNS, KEK, 203-1 Shirakata, Tokai, Ibaraki 319-1106, Japan*

Akira Ohnishi

*Yukawa Institute for Theoretical Physics, Kyoto University, Kyoto 606-8502, Japan*

(Received 13 November 2012; revised manuscript received 4 January 2013; published 25 February 2013)

The excited states of  ${}_{\Lambda}^{25}\text{Mg}$  with the  $\Lambda$  hyperon in  $p$  orbit are studied within the framework of the antisymmetrized molecular dynamics for hypernuclei. We obtained five rotational bands in  ${}_{\Lambda}^{25}\text{Mg}$  in which the  $\Lambda$  hyperon in  $p$  orbit is coupled to the ground and  $K^{\pi} = 2^{+}$  bands of  ${}^{24}\text{Mg}$ . We predict that the corresponding bands of  ${}_{\Lambda}^{25}\text{Mg}$  energetically split due to the triaxial deformation of the core nucleus  ${}^{24}\text{Mg}$  and the spatial anisotropy of the  $p$  orbits of  $\Lambda$ .

DOI: [10.1103/PhysRevC.87.021304](https://doi.org/10.1103/PhysRevC.87.021304)

PACS number(s): 21.80.+a, 21.10.Pc, 27.30.+t

Since a hyperon is unaffected by the Pauli principle governing the nucleons, it can be regarded as an impurity in nuclei and modifies nuclear properties such as clustering and deformation. For example, a  $\Lambda$  hyperon in  $s$  orbit reduces the intercluster distance between  $\alpha$  and  $d$  in  ${}^7_{\Lambda}\text{Li}$ , which was confirmed from the reduction of  $B(E2)$  [1–4]. Furthermore, many authors have predicted the deformation change in  $p$ - $sd$  shell  $\Lambda$  hypernuclei by adding the  $\Lambda$  hyperon in  $s$  orbit [1,2,5–19].

In the case of the  $\Lambda$  hyperon in  $p$  orbit, on which we focus in this study, it can be regarded as a probe of nuclear deformation due to its spatial anisotropy. For example, in  ${}^9_{\Lambda}\text{Be}$ , the splitting of the  $p$  states was predicted due to the axial symmetric deformation ( $2\alpha$  clustering) of  ${}^8\text{Be}$  [5,20]. Namely, the  $\Lambda$  hyperon in  $p$  orbit generates two rotational bands in which  $\Lambda$  moves along the parallel and perpendicular directions of the  $2\alpha$  clustering [20]. In other words, the anisotropy of the  $p$  orbit and axially symmetric deformation of  ${}^8\text{Be}$  lead to the splitting of the  $p$  states. From this fact, we may deduce that the  $p$  states will split into three in the case of triaxial deformation, and we can probe triaxial deformation of the core nucleus by the observation of three different  $p$  states in  $\Lambda$  hypernuclei.

${}^{24}\text{Mg}$  is one of the candidates of triaxially deformed nuclei with the presence of the low-lying  $2^+_2$  state [21–26]. Therefore, we expect that the  $p$  states of  ${}_{\Lambda}^{25}\text{Mg}$  will split into three with different spatial density distribution of the  $\Lambda$  hyperon. To investigate the splitting of  $p$  states of  ${}_{\Lambda}^{25}\text{Mg}$  and its relation to triaxial deformation, we have employed the antisymmetrized molecular dynamics for hypernuclei (HyperAMD) [27]. The HyperAMD with generator coordinate method (GCM) has been successfully applied to investigate the excitation spectra and  $B(E2)$  values of  ${}_{\Lambda}^{25}\text{Mg}$  with the  $\Lambda$  hyperon in  $s$  orbit [28].

The Hamiltonian used in this study is given as

$$\hat{H} = \hat{H}_N + \hat{H}_{\Lambda} - \hat{T}_g, \quad (1)$$

$$\hat{H}_N = \hat{T}_N + \hat{V}_{NN} + \hat{V}_{\text{Coul}}, \quad (2)$$

$$\hat{H}_{\Lambda} = \hat{T}_{\Lambda} + \hat{V}_{\Lambda N}. \quad (3)$$

Here,  $\hat{T}_N$ ,  $\hat{T}_{\Lambda}$ , and  $\hat{T}_g$  are the kinetic energies of nucleons, a  $\Lambda$  hyperon, and the center-of-mass motion, respectively. We have used the Gogny D1S [29] interaction as an effective nucleon-nucleon interaction  $\hat{V}_{NN}$ . The Coulomb interaction  $\hat{V}_{\text{Coul}}$  is approximated by the sum of seven Gaussians. As an effective  $\Lambda N$  interaction  $\hat{V}_{\Lambda N}$ , we have used the central forces of the YNG-NF [30] and YNG-NSC97f [31] interactions with Fermi momentum  $k_F = 1.2 \text{ fm}^{-1}$ , which gives the binding energy of a  $\Lambda$  in  $s$  orbit in  ${}_{\Lambda}^{25}\text{Mg}$ :  $B_{\Lambda} = 16.0 \text{ MeV}$  for YNG-NF, and  $B_{\Lambda} = 12.9 \text{ MeV}$  for YNG-NSC97f. It is found that both YNG-NF and NSC97f interactions give quantitatively the same results. Therefore, the following discussions are based on the results obtained with the YNG-NF interaction.

The intrinsic wave function of a single  $\Lambda$  hypernucleus composed of  $A$  nucleons and a  $\Lambda$  hyperon is described by the parity-projected wave function,  $\Psi^{\pi} = \hat{P}^{\pi} \Psi_{\text{int}}$ , where  $\hat{P}^{\pi}$  is the parity projector and  $\Psi_{\text{int}}$  is the intrinsic wave function given as

$$\Psi_{\text{int}} = \Psi_N \otimes \varphi, \quad \Psi_N = \frac{1}{\sqrt{A!}} \det\{\phi_i(r_j)\}, \quad (4)$$

$$\phi_i = \prod_{\sigma=x,y,z} \left( \frac{2\nu_{\sigma}}{\pi} \right)^{\frac{1}{4}} \exp\{-\nu_{\sigma}(r - Z_i)_{\sigma}^2\} \chi_i \eta_i, \quad (5)$$

$$\varphi = \sum_{m=1}^M c_m \phi_m(\mathbf{r}), \quad (6)$$

$$\phi_m = \prod_{\sigma=x,y,z} \left( \frac{2\nu_{\sigma}}{\pi} \right)^{\frac{1}{4}} \exp\{-\nu_{\sigma}(r - z_m)_{\sigma}^2\} \chi_m, \quad (7)$$

$$\chi_i = \alpha_i \chi_{\uparrow} + \beta_i \chi_{\downarrow}, \quad \chi_m = a_m \chi_{\uparrow} + b_m \chi_{\downarrow}, \quad (8)$$

$$\eta_i = \text{proton or neutron}, \quad (9)$$

where  $\phi_i$  is  $i$ th nucleon single-particle wave packet consisting of spatial, spin  $\chi_i$ , and isospin  $\eta_i$  parts. The single-particle wave function of  $\Lambda$  ( $\varphi$ ) is represented by a superposition of

Gaussian wave packets, which is essential to describe the  $\Lambda$  hyperon in  $p$  orbit. The variational parameters are the centroids of Gaussian  $\mathbf{Z}_i$  and  $\mathbf{z}_m$ , width parameters  $\nu_\sigma$ , spin directions  $\alpha_i$ ,  $\beta_i$ ,  $\alpha_m$ , and  $\beta_m$ , and coefficients  $c_m$ . We approximately remove the spurious center-of-mass kinetic energy in the same way as in Ref. [27].

By using the frictional cooling method, the variation parameters are so determined as to minimize the total energy under the constraints. Two kinds of constraints are simultaneously imposed on the variational calculation. The first is imposed on nuclear quadrupole deformation parameters  $\beta$  and  $\gamma$  to obtain the intrinsic wave functions of  ${}^{25}_\Lambda\text{Mg}$  for given deformation parameters as in our previous work [28]. The other is imposed on the  $\Lambda$  single-particle wave function to obtain  $p$  states by adding the constraint potential,  $V_f = \lambda \sum_f |\varphi_f\rangle\langle\varphi_f|$ , which forbids the  $\Lambda$  hyperon from occupying the orbit  $\varphi_f$  with sufficiently large value of  $\lambda$ . The actual calculational procedure is as follows. First, we perform the variational calculation with the constraint on the nuclear deformation but without the constraint on the  $\Lambda$  single-particle wave function to obtain the lowest energy state of  ${}^{25}_\Lambda\text{Mg}$  for given values of  $\beta$  and  $\gamma$ . Then, denoting the  $\Lambda$  single-particle orbit obtained by this calculation as  $\varphi_1$ , we perform another variational calculation with the second constraint,  $V_f = \lambda|\varphi_1\rangle\langle\varphi_1|$ , as well as the constraint on the nuclear deformation. This variational calculation generates a second lowest energy state whose  $\Lambda$  single-particle wave function is denoted as  $\varphi_2$ , and we complete the calculation for the  $s$ -orbit states. We further proceed in the calculation by adding the constraint  $V_f = \lambda \sum_{f=1,2} |\varphi_f\rangle\langle\varphi_f|$ , which produces the third lowest energy state (i.e., the lowest  $p$  state)  $\varphi_3$ . By continuing this procedure, we obtain two  $s$  orbits ( $\varphi_1$  and  $\varphi_2$ ) and six  $p$  orbits ( $\varphi_3, \dots, \varphi_8$ ).

After the variation, we projected out an eigenstate of the total angular momentum,

$$\Psi_{MKf}^{J\pi}(\beta, \gamma) = \hat{P}_{MK}^J \Psi_f^\pi \quad (10)$$

$$= \hat{P}_{MK}^J \hat{P}^\pi(\Psi_N(\beta, \gamma) \otimes \varphi_f), \quad (11)$$

$$f = 3, 4, \dots, 8, \quad (12)$$

where  $\hat{P}_{MK}^J$  is the total angular momentum projector.

We calculate the mixing among the different  $K$  states that have the same intrinsic deformation  $(\beta, \gamma)$  in the same way as our previous work [28],

$$\Phi_f^{J\pi}(\beta_i, \gamma_i) = \sum_{K=-J}^J f_K \Psi_{MKf}^{J\pi}(\beta_i, \gamma_i), \quad (13)$$

and call it the  $K$ -mixed state. Finally, the  $K$ -mixed states with different deformations  $(\beta_i, \gamma_i)$  and  $p$  states of the  $\Lambda$  hyperon are superposed (GCM),

$$\Phi_\alpha^{J\pi} = \sum_{i,f=3,\dots,8} g_{i,\alpha,f} \Phi_f^{J\pi}(\beta_i, \gamma_i), \quad (14)$$

where quantum numbers other than total angular momentum and parity are represented by  $\alpha$ . The coefficients  $g_{i,\alpha,f}$  and eigenenergies  $E$  are determined by the Hill-Wheeler equation.

We introduce  $B_\Lambda$ , which is the energy difference between the  $J^\pi$  state of  ${}^{25}_\Lambda\text{Mg}$  and the ground state of  ${}^{24}\text{Mg}$ , after the

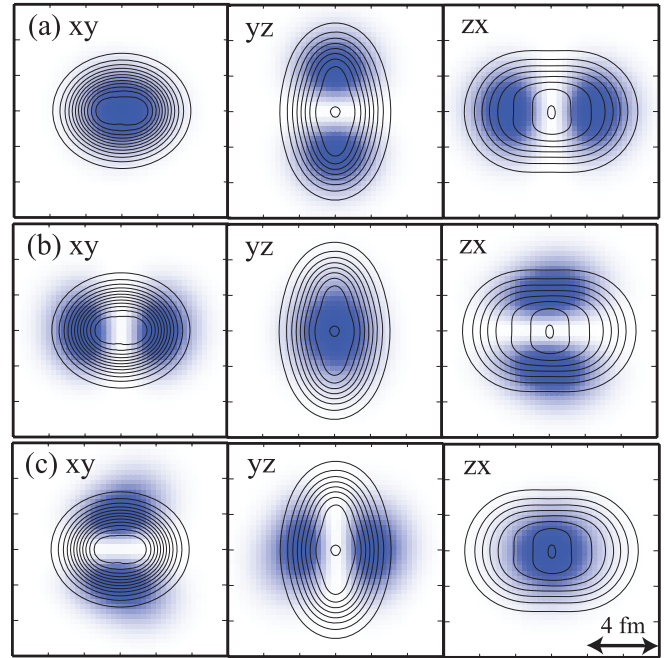


FIG. 1. (Color online) Intrinsic density distributions of (a)  $\varphi_{p1}$ , (b)  $\varphi_{p2}$ , and (c)  $\varphi_{p3}$  at  $(\beta = 0.48, \gamma = 21^\circ)$  which corresponds to the peak of the GCM overlap for the ground state of  ${}^{24}\text{Mg}$ . Contour lines show the nuclear density distributions, while color plots show the distributions of  $\Lambda$  in each panel.

GCM calculation,

$$B_\Lambda = E({}^{24}\text{Mg}(\text{g.s.})) - E({}^{25}_\Lambda\text{Mg}(J^\pi)). \quad (15)$$

To analyze the GCM wave function, we calculate the GCM overlap defined by

$$O_\alpha^{J\pi}(\beta, \gamma) = \max_{f=3,\dots,8} |(\Phi_f^{J\pi}(\beta, \gamma) | \Phi_\alpha^{J\pi})|^2. \quad (16)$$

Since the GCM overlap shows the contribution to the GCM wave function from the  $K$ -mixed states with quadrupole deformation  $(\beta, \gamma)$ , it shows the distribution of the deformation for each excited state.

The  $\Lambda$  single-particle energies as a function of  $\beta$  and  $\gamma$ , which are defined as

$$\epsilon_f(\beta, \gamma) = \langle \Psi_f^\pi(\beta, \gamma) | \hat{H}_N + \hat{H}_\Lambda | \Psi_f^\pi(\beta, \gamma) \rangle - \langle \Psi_N^\pi(\beta, \gamma) | \hat{H}_N | \Psi_N^\pi(\beta, \gamma) \rangle, \quad (17)$$

$$f = 3, 4, \dots, 8, \quad (18)$$

are, of course, twofold degenerate, and hence we obtain three  $p$  states with different spatial distribution which we denote as  $\varphi_{p1}$ ,  $\varphi_{p2}$ , and  $\varphi_{p3}$  in ascending order of their single-particle energies,  $\epsilon_{p1}$  ( $=\epsilon_3 = \epsilon_4$ ),  $\epsilon_{p2}$  ( $=\epsilon_5 = \epsilon_6$ ), and  $\epsilon_{p3}$  ( $=\epsilon_7 = \epsilon_8$ ). Here,  $\Psi_N^\pi(\beta, \gamma) = \hat{P}^\pi \Psi_N(\beta, \gamma)$  is obtained for  ${}^{24}\text{Mg}$  by the energy variation with the  $(\beta, \gamma)$  constraints.

Figure 1 shows the intrinsic density distributions of the  $\varphi_{p1}$ ,  $\varphi_{p2}$ , and  $\varphi_{p3}$ . All of them correspond to the  $p$  orbit, because they have a node. The  $\varphi_{p1}$  is parallel to the longest axis of the nuclear deformation, while  $\varphi_{p2}$  and  $\varphi_{p3}$  are parallel to the middle and shortest axes, respectively. Therefore the magnetic

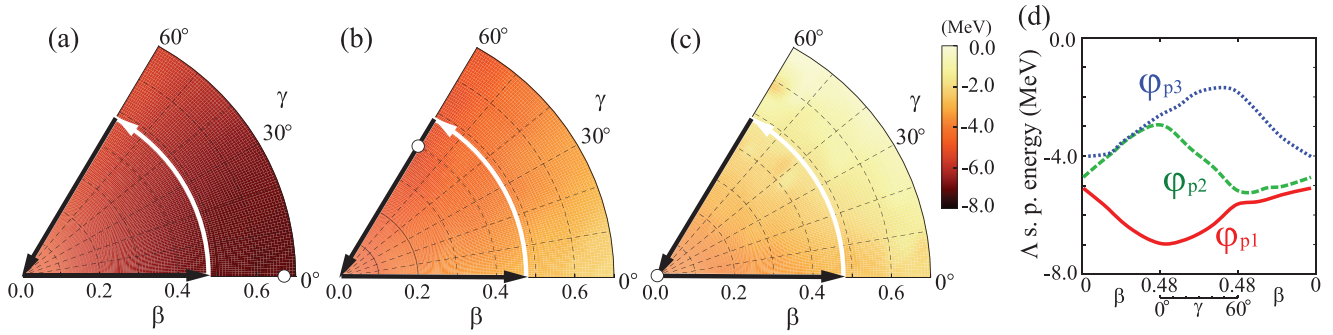


FIG. 2. (Color online)  $\Lambda$  single-particle energy defined by Eq. (17) for (a)  $\varphi_{p1}$ , (b)  $\varphi_{p2}$ , and (c)  $\varphi_{p3}$ . Open circles show the peak of the single-particle energy on the  $(\beta, \gamma)$  plane for each orbit. (d)  $\Lambda$  single-particle energies for  $\varphi_{p1}$  (solid),  $\varphi_{p2}$  (dashed), and  $\varphi_{p3}$  (dotted) along the loop shown in (a)–(c). This loop starts from and heads back to the origin ( $\beta = 0, \gamma = 0^\circ$ ) via  $(\beta = 0.48, \gamma = 0^\circ)$  and  $(\beta = 0.48, \gamma = 60^\circ)$ .

quantum number of the orbital angular momentum of each  $\Lambda$  hyperon,  $l_z$ , is  $l_z = 0$  for  $\varphi_{p1}$  and  $l_z = 1$  for  $\varphi_{p2}$  and  $\varphi_{p3}$ .

The single-particle energies of the  $\Lambda$  hyperon ( $\epsilon_{p1}$ ,  $\epsilon_{p2}$ , and  $\epsilon_{p3}$ ) as function of  $\beta$  and  $\gamma$  are shown in Figs. 2(a)–2(c). Their behaviors are different from each other, i.e., the  $\epsilon_{p1}$  has a minimum with prolate deformation [ $\epsilon_{p1}(\beta = 0.68, \gamma = 2^\circ) = -7.15$  MeV], while  $\epsilon_{p2}$  and  $\epsilon_{p3}$  have oblate and spherical minima [ $\epsilon_{p2}(\beta = 0.40, \gamma = 57^\circ) = -5.26$  MeV,  $\epsilon_{p3}(\beta = 0.0) = -4.02$  MeV], respectively. The dependences of the  $\Lambda$  single-particle energies on the nuclear quadrupole deformation are clearly seen in Fig. 2(d), where they are plotted along the path on the  $(\beta, \gamma)$  plane shown in Figs. 2(a)–2(c). At prolate deformation ( $\gamma = 0^\circ$ ),  $\varphi_{p1}$  is most deeply bound, and  $\varphi_{p2}$  and  $\varphi_{p3}$  are energetically degenerated. This is similar to the  $p$  states of  ${}^9\text{Be}$  where the  $\varphi_{p1}$  corresponds to the lowest  $p$  state, the so-called supersymmetric [5] (or genuine hypernuclear [20]) state. With oblate deformation ( $\gamma = 60^\circ$ ),  $\varphi_{p1}$  and  $\varphi_{p2}$  are degenerate, and  $\varphi_{p3}$  which is parallel to the symmetric axis of the deformation is more weakly bound than the others. In the triaxially deformed region ( $0^\circ < \gamma < 60^\circ$ ), the  $\Lambda$  single-particle energies are different from each other for  $\varphi_{p1}$ ,  $\varphi_{p2}$ , and  $\varphi_{p3}$  due to triaxial deformation. Thus, the  $p$  states split into two with axially symmetric deformation and they split into three with triaxial deformation. Therefore we can expect that three  $p$  states appear in  ${}^{25}_\Lambda\text{Mg}$ . However, the above discussions neglect the energy of the nucleon part which is also changed as function of  $\beta$  and  $\gamma$ , and we need to take it

into account by performing the GCM calculation. It is noted that the  $\Lambda$  binding energy  $B_\Lambda$  is different from the absolute value of  $\epsilon_f(\beta, \gamma)$ . Their definitions are quite different from each other. In Eq. (17),  $\epsilon_f(\beta, \gamma)$  is defined as the difference between the intrinsic energies of  ${}^{25}_\Lambda\text{Mg}$  and  ${}^{24}\text{Mg}$  for each  $(\beta, \gamma)$ , while  $B_\Lambda$  [Eq. (15)] is the energy difference between each state of  ${}^{25}_\Lambda\text{Mg}$  and the  ${}^{24}\text{Mg}$  ground state after the angular momentum projection and GCM calculation, which should be compared with the observations.

Figures 3(a)–3(b) show the excitation spectra of  ${}^{24}\text{Mg}$  and  ${}^{25}_\Lambda\text{Mg}$ , respectively, obtained with the GCM calculation. Excitation energies of the band head states are listed in Table I. It is expected that an  $\alpha + {}^{21}_\Lambda\text{Ne}$  decay channel is the lowest threshold lying in between 8.3 and 12.5 MeV, which is estimated from the observed  $B_\Lambda$  values of  ${}^{16}_\Lambda\text{O}$  [11,32] and  ${}^{28}_\Lambda\text{Si}$  [33]; i.e., we assume that  $B_\Lambda$  of  ${}^{21}_\Lambda\text{Ne}$  is in between them. Therefore, some of the  $p$  states may be bound. Five rotational bands are obtained as the  $p$  states of  ${}^{25}_\Lambda\text{Mg}$ . They are generated by the coupling of the  $\Lambda$  hyperon in  $p$  orbit ( $\varphi_{p1}$ ,  $\varphi_{p2}$ , and  $\varphi_{p3}$ ) to the ground and  $K^\pi = 2^+$  side bands of  ${}^{24}\text{Mg}$ . Coupling of  $\varphi_{p1}$ ,  $\varphi_{p2}$ , and  $\varphi_{p3}$  to the ground band of  ${}^{24}\text{Mg}$  generates the three bands built on the  $(1/2^-_1, 3/2^-_1)$ ,  $(1/2^-_2, 3/2^-_2)$ , and  $(1/2^-_3, 3/2^-_3)$  states, respectively. In the lowest band built on the  $(1/2^-_1, 3/2^-_1)$  states, the contribution from  $\varphi_{p1}$  to the GCM wave function is dominant, and the distribution of the GCM overlap as functions of  $\beta$  and  $\gamma$  is similar to the ground band of  ${}^{24}\text{Mg}$  as shown in Fig. 4. Therefore, we call it  $\text{GB} \otimes \varphi_{p1}$ , where

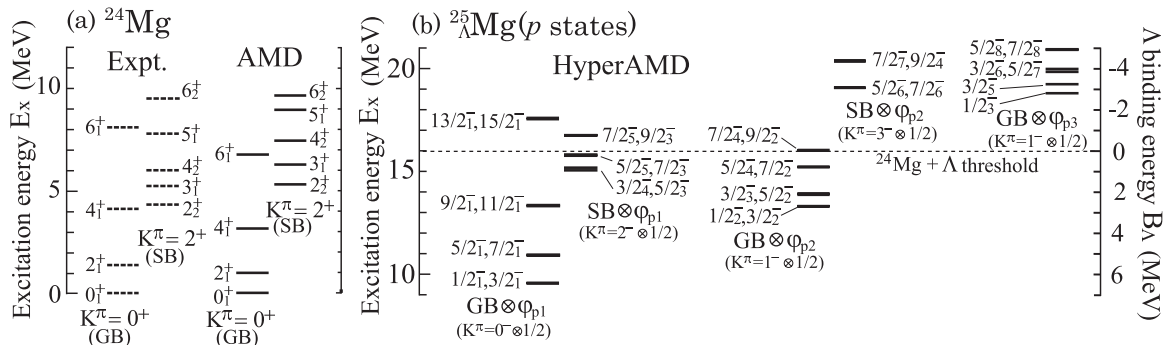


FIG. 3. Calculated excitation spectra of the ground band  $K^\pi = 0^+$  and side band  $K^\pi = 2^+$  of  ${}^{24}\text{Mg}$  (a), and the  $p$  states of  ${}^{25}_\Lambda\text{Mg}$  (b). The dashed line in (b) shows the  ${}^{24}\text{Mg} + \Lambda$  threshold energy calculated by Eq. (15).

TABLE I. Excitation energies ( $E_x$ ) and  $B_\Lambda$  defined by Eq. (15) of each state in  $^{25}_\Lambda\text{Mg}$  ( $E_x$  and  $B_\Lambda$  in MeV). ( $\beta$ ,  $\gamma$ ) corresponding to the peak of the GCM overlap are also listed ( $\gamma$  in degrees).

Configuration	$J^\pi$	$E_x$	$B_\Lambda$	$\beta$	$\gamma$	Configuration	$J^\pi$	$E_x$	$B_\Lambda$	$\beta$	$\gamma$
$^{24}\text{Mg}(0_1^+) \otimes \varphi_{p1}$	$1/2_1^-$	9.55	6.43	0.48	21	$^{24}\text{Mg}(2_1^+) \otimes \varphi_{p1}$	$5/2_1^-$	10.90	5.08	0.48	21
$^{24}\text{Mg}(0_1^+) \otimes \varphi_{p2}$	$1/2_2^-$	13.30	2.68	0.43	15	$^{24}\text{Mg}(2_1^+) \otimes \varphi_{p2}$	$5/2_4^-$	15.20	0.78	0.45	31
$^{24}\text{Mg}(0_1^+) \otimes \varphi_{p3}$	$1/2_3^-$	18.80	-2.82	0.53	27	$^{24}\text{Mg}(2_1^+) \otimes \varphi_{p3}$	$5/2_8^-$	20.91	-4.93	0.64	41
$^{24}\text{Mg}(2_2^+) \otimes \varphi_{p1}$	$5/2_3^-$	15.05	0.93	0.53	27						
$^{24}\text{Mg}(2_2^+) \otimes \varphi_{p2}$	$5/2_6^-$	19.08	-3.10	0.48	21						

GB denotes the ground band of  $^{24}\text{Mg}$ . Since the bands built on the  $(1/2_2^-, 3/2_2^-)$  and  $(1/2_3^-, 3/2_5^-)$  states have the largest contributions from  $\varphi_{p2}$  and  $\varphi_{p3}$ , respectively, and  $\varphi_{p1}$  does not contribute to these bands, we call them  $\text{GB} \otimes \varphi_{p2}$  and  $\text{GB} \otimes \varphi_{p3}$ . Therefore, the  $p$  states coupled to the ground band of  $^{24}\text{Mg}$  split into three bands. The  $p$  states coupled to the  $K^\pi = 2^+$  band of  $^{24}\text{Mg}$  are built on the  $(3/2_4^-, 5/2_3^-)$  and  $(5/2_6^-, 7/2_6^-)$  states having the largest contributions from  $\varphi_{p1}$  and  $\varphi_{p2}$ , respectively, which we call  $\text{SB} \otimes \varphi_{p1}$  and  $\text{SB} \otimes \varphi_{p2}$ . We do not obtain the  $\text{SB} \otimes \varphi_{p3}$  band generated by the coupling between  $\varphi_{p3}$  and  $K^\pi = 2^+$  band of  $^{24}\text{Mg}$  in this calculation. The  $B(E2)$  values also support this band classification. Namely, the  $B(E2)$  values are larger for the intraband transitions as shown in Table II, while the interband  $B(E2)$  values are rather small ( $\leq 10 e^2\text{fm}^2$ ).

The band structure of the  $p$  states shown in Fig. 3(b) is approximately understood by the strong coupling between the magnetic quantum numbers of  $^{24}\text{Mg}$  ( $J_z$ ) and the orbital angular momentum of  $\Lambda$  ( $l_z$ ). Since  $l_z = 0$  for  $\varphi_{p1}$ , coupling of  $\varphi_{p1}$  to the ground band of  $^{24}\text{Mg}$  generates a  $K^\pi = 0^-$

band which has band members,  $1^-, 3^-, 5^-, \dots$  states, without spin  $1/2$  of  $\Lambda$ . Each doublet of the  $\text{GB} \otimes \varphi_{p1}$  band, such as  $(1/2_1^-, 3/2_1^-)$ , is generated by the weak coupling of the spin of  $\Lambda$  to the band members of the  $K^\pi = 0^-$  band. Similarly, the  $\text{SB} \otimes \varphi_{p1}$  band is understood as the  $K^\pi = 2^-$  band without the spin  $1/2$  of  $\Lambda$ , due to the coupling of  $\varphi_{p1}$  ( $l_z = 0$ ) to the side band  $K^\pi = 2^+$  of  $^{24}\text{Mg}$ . For  $\varphi_{p2}$  and  $\varphi_{p3}$  with  $l_z = 1$ , coupling of  $l_z = 1$  to the ground band of  $^{24}\text{Mg}$  generates the  $K^\pi = 1^-$  bands as the  $\text{GB} \otimes \varphi_{p2}$  and  $\text{GB} \otimes \varphi_{p3}$  bands. The  $\text{SB} \otimes \varphi_{p2}$  band is also explained by the strong-coupling picture in which the  $K^\pi = 1^-$  and  $K^\pi = 3^-$  bands should exist. In this work, only the  $K^\pi = 3^-$  band appears in Fig. 3(b), which is because each state of the  $K^\pi = 1^-$  band of  $\text{SB} \otimes \varphi_{p2}$  is mixed with the  $\text{GB} \otimes \varphi_{p3}$  band which is also the  $K^\pi = 1^-$  band. By analysis of the GCM overlap, it is found that the  $\text{GB} \otimes \varphi_{p3}$  band has a sizable amount of  $\varphi_{p2}$  components (about 20% at maximum), while the contributions from  $\varphi_{p3}$  are larger (about 40% at maximum). It is noted that the band structure of  $\text{GB} \otimes \varphi_{p1}$  and  $\text{GB} \otimes \varphi_{p2}$  is similar to the  $p$  states of  $^9_\Lambda\text{Be}$  predicted by Ref. [20], because the prolate deformation is important for  $^{25}_\Lambda\text{Mg}$  as well as triaxial deformation. Indeed, the GCM overlap is maximized at  $(\beta = 0.48, \gamma = 22^\circ)$  for the ground state of  $^{24}\text{Mg}$  as shown in Fig. 4(a).

We also investigate the deformation change of the  $^{24}\text{Mg}$  ground state, due to the  $\Lambda$  hyperon in  $p$  orbit. Figure 4 shows the distributions of the GCM overlap, defined by Eq. (16), for the  $1/2_1^-, 1/2_2^-$ , and  $1/2_3^-$  states of  $^{25}_\Lambda\text{Mg}$  as well as the ground state  $0^+$  of  $^{24}\text{Mg}$ . The  $(\beta, \gamma)$  value corresponding to the peak of the GCM overlap is presented in Table I for each state. It is found that  $\varphi_{p1}$  keeps the triaxial deformation of the  $^{24}\text{Mg}$  ground state unchanged, while  $\varphi_{p2}$  slightly reduces it. Indeed, the peak of the GCM overlap for the  $1/2_1^-$  state locates at the same position as the  $^{24}\text{Mg}$  ground state ( $\beta = 0.48, \gamma = 21^\circ$ ). This is because  $\varphi_{p1}$  is more deeply bound in the prolate deformed region as shown in Fig. 2(a). This trend of  $\varphi_{p1}$  is different from the  $\Lambda$  hyperon in  $s$  orbit which reduces the nuclear deformation [18,19,28]. On the other hand, the deformation of the  $1/2_2^-$  state is changed to  $(\beta, \gamma) = (0.43, 15^\circ)$  by  $\varphi_{p2}$ , while the behavior of Fig. 2(b) shows that  $\varphi_{p2}$  is deeply bound with oblate deformation. This is because the energy surface of the  $^{24}\text{Mg}$  ground state is steep in the oblate side.

For the  $1/2_3^-$  state corresponding to  $\varphi_{p3}$ , the distribution of the GCM overlap is quite different from the  $1/2_1^-$  and  $1/2_2^-$  states. Figure 4 and Table I show that the peak of the GCM overlap for the  $1/2_3^-$  state locates at  $(\beta, \gamma) = (0.45, 31^\circ)$ , and the  $1/2_3^-$  state has almost no component

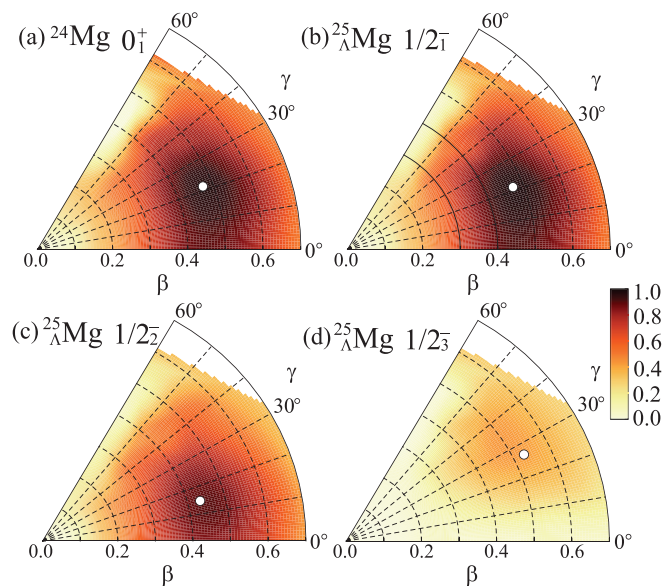


FIG. 4. (Color online) Color plot (grayscale) shows the distribution of the GCM overlap. The definition of the GCM overlap is given by Eq. (16). (a)–(d) correspond to the ground state  $0^+$  of  $^{24}\text{Mg}$  and the band head states  $1/2_1^-$ ,  $1/2_2^-$ , and  $1/2_3^-$  of  $^{25}_\Lambda\text{Mg}$ , respectively. Open circles represent the peak positions of the GCM overlap for each state.

TABLE II. Intradband  $B(E2)$  values in units of  $e^2\text{fm}^4$ .

GB $\otimes \varphi_{p1}$		GB $\otimes \varphi_{p2}$		GB $\otimes \varphi_{p3}$		SB $\otimes \varphi_{p1}$		SB $\otimes \varphi_{p2}$	
Transitions	$B(E2)$	Transitions	$B(E2)$	Transitions	$B(E2)$	Transitions	$B(E2)$	Transitions	$B(E2)$
$5/2_1^- \rightarrow 1/2_1^-$	95	$3/2_3^- \rightarrow 1/2_2^-$	73	$3/2_6^- \rightarrow 1/2_3^-$	66	$5/2_5^- \rightarrow 3/2_4^-$	145	$7/2_7^- \rightarrow 5/2_6^-$	139
$7/2_1^- \rightarrow 3/2_1^-$	122	$5/2_2^- \rightarrow 3/2_2^-$	116	$5/2_7^- \rightarrow 3/2_5^-$	103	$7/2_3^- \rightarrow 5/2_3^-$	161	$9/2_5^- \rightarrow 7/2_6^-$	150
$9/2_1^- \rightarrow 5/2_1^-$	127	$5/2_4^- \rightarrow 3/2_3^-$	37	$5/2_8^- \rightarrow 3/2_6^-$	51	$7/2_5^- \rightarrow 5/2_5^-$	111		
$11/2_1^- \rightarrow 7/2_1^-$	136	$7/2_2^- \rightarrow 5/2_2^-$	42	$7/2_8^- \rightarrow 5/2_7^-$	57	$9/2_3^- \rightarrow 7/2_3^-$	124		
		$5/2_4^- \rightarrow 1/2_2^-$	52	$5/2_8^- \rightarrow 1/2_3^-$	57				
		$7/2_2^- \rightarrow 3/2_2^-$	65	$7/2_8^- \rightarrow 3/2_5^-$	72				

in axially deformed region. This is consistent with the fact that the  $1/2_3^-$  state is generated due to the nuclear triaxial deformation of  $^{25}_{\Lambda}\text{Mg}$ , originating in the energy splitting of the  $\Lambda$  single-particle energy with triaxial deformation as shown in Fig. 2(d).

In summary, we have investigated the level structure of the  $p$  states in  $^{25}_{\Lambda}\text{Mg}$  based on the HyperAMD calculation. We have employed the constraints on the single-particle wave function of  $\Lambda$  as well as on  $(\beta, \gamma)$  deformation, and obtained three intrinsic  $p$  states with different spatial density distributions. By performing the GCM calculation, five bands are obtained

as the  $p$  states of  $^{25}_{\Lambda}\text{Mg}$ . It is found that three of them are generated by the coupling of the ground band of  $^{24}\text{Mg}$  and  $\Lambda$  in each  $p$  orbit. Therefore the  $p$  state of  $^{25}_{\Lambda}\text{Mg}$  will split into three due to triaxial deformation.

This work is supported in part by the Grants-in-Aid for Scientific Research on Innovative Areas from MEXT (No. 2404: 24105001, 24105008), and by a Grant-in-Aid from the Japan Society for the Promotion of Science (No. 236937). The authors thank the J-PARC Branch of KEK Theory Center for partially supporting this work.

- [1] H. Bandō, *Nucl. Phys. A* **450**, 217c (1986).  
[2] E. Hiyama, M. Kamimura, K. Miyazaki, and T. Motoba, *Phys. Rev. C* **59**, 2351 (1999).  
[3] H. Tamura, K. Tanida, D. Abe, H. Akikawa, K. Araki, H. Bhang, T. Endo, Y. Fujii, T. Fukuda, O. Hashimoto *et al.*, *Phys. Rev. Lett.* **84**, 5963 (2000).  
[4] K. Tanida, H. Tamura, D. Abe, H. Akikawa, K. Araki, H. Bhang, T. Endo, Y. Fujii, T. Fukuda, O. Hashimoto *et al.*, *Phys. Rev. Lett.* **86**, 1982 (2001).  
[5] R. H. Dalitz and A. Gal, *Phys. Rev. Lett.* **36**, 362 (1976).  
[6] T. Motoba, H. Bandō, and K. Ikeda, *Prog. Theor. Phys.* **70**, 189 (1983).  
[7] T. Yamada, K. Ikeda, H. Bandō, and T. Motoba, *Prog. Theor. Phys.* **71**, 985 (1984).  
[8] T. Motoba, H. Bandō, K. Ikeda, and T. Yamada, *Prog. Theor. Phys. Suppl.* **81**, 42 (1985).  
[9] D. J. Millener, *Nucl. Phys. A* **691**, 93c (2001).  
[10] K. Itonaga, T. Motoba, O. Richter, and M. Sotona, *Phys. Rev. C* **49**, 1045 (1994).  
[11] O. Hashimoto and H. Tamura, *Prog. Part. Nucl. Phys.* **57**, 564 (2006).  
[12] X.-R. Zhou, H.-J. Schulze, H. Sagawa, C.-X. Wu, and E.-G. Zhao, *Phys. Rev. C* **76**, 034312 (2007).  
[13] M. T. Win and K. Hagino, *Phys. Rev. C* **78**, 054311 (2008).  
[14] D. Millener, *Nucl. Phys. A* **804**, 84 (2008).  
[15] K. Hagino, M. T. Win, and Y. Nakagawa, *Int. J. Mod. Phys. E* **19**, 2552 (2010).  
[16] H.-J. Schulze, M. T. Win, K. Hagino, and H. Sagawa, *Prog. Theor. Phys.* **123**, 569 (2010).  
[17] M. Isaka, M. Kimura, A. Doté, and A. Ohnishi, *Phys. Rev. C* **83**, 044323 (2011).  
[18] M. T. Win, K. Hagino, and T. Koike, *Phys. Rev. C* **83**, 014301 (2011).  
[19] J. M. Yao, Z. P. Li, K. Hagino, M. T. Win, Y. Zhang, and J. Meng, *Nucl. Phys. A* **868**, 12 (2011).  
[20] H. Bandō, M. Seki, and Y. Shōno, *Prog. Theor. Phys.* **66**, 2118 (1981).  
[21] R. Batchelor, A. Ferguson, H. Gove, and A. Litherland, *Nucl. Phys.* **16**, 38 (1960).  
[22] A. Cohen and J. Cookson, *Nucl. Phys.* **29**, 604 (1962).  
[23] M. Girod and B. Grammaticos, *Phys. Rev. C* **27**, 2317 (1983).  
[24] M. Bender and P.-H. Heenen, *Phys. Rev. C* **78**, 024309 (2008).  
[25] T. R. Rodríguez and J. L. Egido, *Phys. Rev. C* **81**, 064323 (2010).  
[26] M. Kimura, R. Yoshida, and M. Isaka, *Prog. Theor. Phys.* **127**, 287 (2012).  
[27] M. Isaka, M. Kimura, A. Doté, and A. Ohnishi, *Phys. Rev. C* **83**, 054304 (2011).  
[28] M. Isaka, H. Homma, M. Kimura, A. Doté, and A. Ohnishi, *Phys. Rev. C* **85**, 034303 (2012).  
[29] J. Dechargé and D. Gogny, *Phys. Rev. C* **21**, 1568 (1980).  
[30] Y. Yamamoto, T. Motoba, H. Himeno, K. Ikeda, and S. Nagata, *Prog. Theor. Phys. Suppl.* **117**, 361 (1994).  
[31] Y. Yamamoto (private communication).  
[32] S. Ajimura, K. Aoki, H. Bhang, T. Endo, Y. Fujii, O. Hashimoto, H. Hotchi, E. Hungerford, J. Kim, Y. Kim *et al.*, *Nucl. Phys. A* **639**, 93c (1998).  
[33] T. Hasegawa, O. Hashimoto, S. Homma, T. Miyachi, T. Nagae, M. Sekimoto, T. Shibata, H. Sakaguchi, T. Takahashi, K. Aoki *et al.*, *Phys. Rev. C* **53**, 1210 (1996).